Sensors and Materials, Vol. 38, No. 7 (2026) 4141–4158
MYU Tokyo

S & M 4555

Analysis of Thermal Behavior in Liquid-cooling Battery Systems for Electric Vehicles Exposed to Solar Irradiance

Zhiyong Deng,[1] Chi-Hsin Yang,[1*] Long Wu,[1] Yingqun Cai,[1] and Jizu Zhang[2]

[1]School of Mechanical and Electric Engineering, Sanming University, Sanming, Fujian Province 365004, China
[2]FEV Group GmbH, Aachen, Germany

(Received May 11, 2026; accepted July 1, 2026)

Keywords: lithium-ion battery, solar irradiance, liquid cooling, thermal analysis

In this study, we report a three-dimensional thermal-fluid-coupled finite element model (FEM) for a lithium-ion-battery liquid-cooling system, explicitly incorporating solar irradiance as a boundary condition. The model is validated computationally and used to investigate the pack's thermal behavior under solar exposure. Two designs of the cooling architecture, focusing on flow channel geometry and manifold configuration, are proposed to enhance thermal management. Numerical analysis shows that the designs significantly improve performance. At an ambient temperature of 35 ℃, the optimized design reduces the maximum and average volumetric temperatures by 40.91 and 48.64%, respectively, compared with a reference configuration. It also achieves a peak temperature reduction of 25.42 ℃ under 2C discharge. We conclude that solar heating can raise the casing temperature of a pack to 79 ℃, driving inward heat conduction, and that optimizing inlet geometry to shorten flow paths is effective in mitigating axial temperature gradients. Furthermore, we propose the present simulation methodology as a practical, time-efficient alternative to year-long outdoor aging tests for battery thermal and degradation evaluation, enabling accelerated testing with rationally selected environmental profiles.

1. Introduction

Driven by technological progress in electric vehicles (EVs), strengthened governmental incentives, and growing global commitments to sustainability, research into EV battery systems has become indispensable for accelerating the adoption and performance enhancement of electricity-powered mobility. As sustainable transport transitions gain momentum, the effective thermal regulation of lithium-ion battery packs has assumed central importance in EV engineering, significantly contributing to overall energy utilization efficiency while safeguarding operational integrity and long-term reliability.[(1)]

Emerging research by Yue *et al.*[(2)] highlighted that breakthroughs in novel thermal interface materials and optimized battery thermal management system (BTMS) architectures play a pivotal role in suppressing excessive thermal buildup associated with battery charge or discharge

[*]Corresponding author: e-mail: 20190207@fjsmu.edu.cn
https://doi.org/10.18494/SAM6407

ISSN 0914-4935 © MYU K.K.
https://myukk.org/

operations. Such thermal regulation capabilities become indispensable when deployed in applications characterized by elevated power density and rapid current delivery. In a recent study,[3] the evolution of lithium-ion BTMS in electric mobility platforms was critically examined, focusing on three principal heat dissipation approaches, namely, convective air cooling, forced liquid circulation, and latent-heat absorption using phase change materials (PCMs). Complementing this, Vinten *et al.*[4] developed a time-resolved, full-vehicle simulation framework to rigorously characterize both transient temperature evolution and parasitic energy losses within battery packs across standardized driving profiles reflective of actual usage conditions.

In the domain of thermal regulation for battery packs, Tan *et al.*[5] explored how heat generation mechanisms in lithium-ion cells evolve under diverse charging and discharging conditions, while also quantifying how ambient temperature modulates thermal dynamics during cycling. Fan *et al.*[6] developed a hybrid cooling approach that integrates liquid-based heat removal with PCMs and validated its performance through the simulation-based analysis of high-energy-density cells operating under multiple ambient thermal conditions. Li *et al.*[7] focused on the role of cooling plate architecture in achieving uniform temperature distribution within liquid-cooling modules; leveraging high-fidelity computational models and systematic parametric studies, they benchmarked the thermal efficiency of three distinct structural layouts, namely, convex, honeycomb, and U-channel geometries. Indraneel and Milankumar[8] carried out controlled experimental tests to characterize how fluctuations in surrounding temperature affect not only the thermal profile but also the electrochemical signatures, including voltage and current responses, of $LiFePO_4$ batteries.

Contemporary investigations into the behavior of an energy harvester, such as a battery pack, have prioritized the deployment of sensor systems for continuous, multiparameter monitoring, particularly of indicators linked to performance decay in the battery aging phenomenon. Schreiber *et al.*[9] implemented a trimodal sensing architecture (voltage, current, and temperature) to track terminal potential, bidirectional current flow, and volumetric mean temperature across the pack, supporting the derivation of dynamic load profiles reflective of actual vehicle usage patterns. Hernández *et al.*[10] combined analogous sensing modalities at the individual cell level to record not only electrical variables (voltage and current) but also thermal boundary conditions (surface temperature) and impedance characteristics (internal resistance), laying the groundwork for coupled electrochemical–thermal modeling. Moreover, with regard to thermal regulation in EV battery systems, Pakštys *et al.*[11] installed an array of thermistors at thermally sensitive zones inside the pack to map evolving temperature fields during standardized constant-current discharge tests. Xu *et al.*[12] utilized a spatially resolved temperature monitoring setup to resolve both module-to-module and cell-to-cell thermal heterogeneities under operational conditions, and corroborated their computational thermal model's fidelity through empirical benchmarking. Falcone *et al.*[13] devised an experimental framework based on thermally representative dummy cells, which is equipped with precisely tuned resistive elements to replicate time-varying heat generation, and synchronized high-precision thermal measurements, allowing for the rigorous, scenario-based evaluation of immersion cooling efficacy.

Power battery safety is strongly affected by ambient thermal conditions driven by solar radiation, airflow-induced convection, and humidity. The SAE standards J2464 and J2566 define aging protocols for automotive systems under harsh environmental conditions.[14,15] However, these standards primarily target the degradation of cabin and body materials owing to solar exposure. They provide minimal direction for battery-specific testing, especially regarding solar absorption by battery enclosures. Crucially, they lack methods to quantify real-time temperature changes in cells and modules during solar exposure.

To systematically investigate how ambient conditions, such as solar irradiance, relative humidity, and airflow velocity, affect both thermal dynamics and degradation processes in battery packs, researchers have widely adopted spatially distributed temperature sensing across pack surfaces. Feng *et al.*[16] developed a data-driven aging forecasting model, leveraging temporal patterns identified over extended cycling life and fusing synchronized measurements of voltage, temperature, and current to deliver an integrated assessment of degradation progression. Li *et al.*[17] redesigned the sensor network topology for grid-scale battery installations, facilitating the real-time, high-resolution mapping of interdependent electrical and thermal fields. Chen *et al.*[18] offered an in-depth appraisal of fiber grating sensors applied to lithium-ion batteries, focusing specifically on their capability for the selective, high-fidelity monitoring of individual physical quantities such as thermal and mechanical responses. Kovács *et al.*[19] delved into the intrinsic heat dissipation pathways of 21700 cylindrical lithium-ion cells, characterizing how internal thermal gradients evolve dynamically under diverse environmental temperatures and operational charging or discharging profiles. Finally, Kumba *et al.*[20] uncovered the physicochemical origins of capacity loss and service-life decline, establishing quantitative relationships between key usage factors, such as discharge depth and cycle protocol, and the resulting degradation rates across battery pack assemblies.

Motivated by the previous works, in this study, we investigate the thermal behavior of a power battery liquid-cooling pack under solar irradiation, a critical yet understudied condition in real-world EV operation. We identify gaps in current accelerated aging tests, which lack solar-calibrated thermal boundary conditions and simulation parameters. This work highlights the insufficient understanding of coupled heat transfer and coolant flow under combined high ambient temperature and intense solar flux. It emphasizes that outdoor solar exposure creates nonuniform heating and flow disruption, unlike controlled lab environments. In this research, we aim to establish a computational supported basis for next-generation thermal management system design and validation.

Battery pack thermal safety and aging are traditionally evaluated via time-consuming, costly destructive tests with poor reproducibility and scattered data. To overcome these drawbacks, we introduced an efficient numerical modeling approach for the rapid prediction of the internal and external thermal flow characteristics of battery packs. The method enables physics-guided thermal analysis early in design, reducing dependence on repeated physical testing. We cut down the number of prototype iterations and shortened development cycles. Testing costs were significantly reduced as a result.

In this study, we address the core thermal management challenges for battery packs. However, owing to length constraints, the following critical knowledge gaps were not discussed: (1) transient thermal analysis under active cooling, (2) the experimental characterization and temperature-dependent constitutive modeling of key materials, (3) high-fidelity radiation modeling, including solar spectral irradiance and angular dependence, (4) the multi-physics coupling of thermal-fluid dynamics in cooling channels with the pack's thermal field, (5) integrated electrochemical–thermal–mechanical modeling linking aging to thermomechanical finite-element coupling, and (6) comprehensive model validation against targeted experiments. These are priority research thrusts for upcoming work and will be systematically addressed in subsequent phases.

This paper is structured into four main components. In Sect. 2, we present the development of a three-dimensional thermal-fluid coupled finite element model for a liquid-cooling lithium-ion battery pack, explicitly incorporating solar irradiance as a key boundary condition. In Sect. 3, we describe in detail a systematic numerical investigation into the thermal behavior of the battery pack under solar exposure, followed by computational validation to ensure model fidelity. In Sect. 4, we introduce a targeted redesign of the battery pack's liquid-cooling architecture, focusing on flow channel geometry and manifold configuration, to enhance thermal management efficiency. In the concluding section, we synthesize the principal findings and highlight their implications for practical battery thermal design.

2. Finite Element Analysis of Liquid-cooling Lithium-ion Battery Pack System

2.1 Model subjected to solar radiation

Lithium-ion batteries generate heat internally during charging and discharging, and simultaneously exchange heat with the environment via conduction, radiation, and convection. External heat inputs include solar irradiance and terrestrial longwave radiation, absorbed by the enclosure and conducted inward. Heat is removed mainly through natural or forced convection. Each battery cell's heat transfer results from three components, namely, the internal Joule overpotential heating, net radiative gain, and interfacial heat transfer with surroundings. A thermal balance equation models this behavior as follows.

$$m_i c_i \frac{dT_i}{dt} = Q_{z,i} + Q_{sun,i} + Q_{rad,i} + Q_{cond,i} + Q_{conv,i} \tag{1}$$

In Eq. (1), m_i, c_i, and T_i denote the mass, specific heat capacity, and temperature of the ith grid cell, respectively. $Q_{z,i}$ represents the total volumetric heat transfer within the ith grid cell attributable to electrochemical reactions in the lithium-ion battery during operation. $Q_{sun,i}$ denotes the solar radiative heat absorbed by the ith grid cell. $Q_{rad,i}$, $Q_{cond,i}$, and $Q_{conv,i}$ represent the heat transfer associated with thermal radiation, conduction, and convection, occurring between the ith grid cell and both internal and external environments, respectively.

The radiative heat transfer $Q_{rad,i}$ comprises three components, namely, the ground-reflected radiation absorbed by the *i*th grid cell, the radiation reflected from neighboring grid cells, and the radiation self-emitted by the *i*th grid cell. The conductive heat transfer $Q_{cond,i}$ represents the net conductive heat transfer into the *i*th grid cell, defined as the difference between incoming and outgoing conductive heat. The convective heat transfer $Q_{conv,i}$ denotes the net heat exchange between the *i*th grid cell and the surrounding medium via convection, i.e., the difference between convective heat absorption and dissipation.

The total heat transfer, denoted as $Q_Z = \sum Q_{Z,i}$, within a lithium-ion battery pack during operation arises from four primary thermal contributions, collectively expressed as $Q_z = Q_r + Q_j + Q_p + Q_s$. Specifically, Q_r denotes the reversible reaction heat, Q_j is the irreversible Joule heat, Q_p is the polarization heat associated with electrode kinetics and mass transport limitations, and Q_s represents the heat transfer by parasitic side reactions. In practice, these individual heat components cannot be measured or calculated directly with sufficient accuracy owing to strong coupling among electrochemical and thermal processes, as well as limitations in sensor resolution and model fidelity.[21,22]

On the basis of the findings reported in Refs. 23–26, under conditions of a stable thermal source and uniform spatial distribution of the battery pack, the heat transfer of individual grid cells is derived from the overall heat transfer model for the battery pack during operation. The corresponding expression is given as

$$Q_z = \sum Q_{z,i} = \frac{1}{V_b}\left[(E_0 - U_1) + T\frac{dE_0}{dT}\right]. \tag{2}$$

Equation (2) incorporates the following physical quantities: Q_z is the total heat transfer per unit volume of the battery pack and V_b is the volume per cell. E_0 and U_1 are the open-circuit and terminal voltages of an individual cell, respectively. T is the ambient temperature and dE_0/dT is a coefficient reflecting the thermal sensitivity of the battery. According to the existing experimental evidence, the reversible reaction heat $T(dE_0/dT)$ contributes insignificantly to the overall thermal budget and is therefore omitted in this modeling framework.[27]

In Eq. (2), the term $E_0 - U_1$ can be substituted with $E_0 - U_1 = I^2R_0$. Here, I denotes the discharge or charge current of the individual battery cell, and its magnitude is given by the product of the cell's capacitance and the corresponding discharge or charge rate. R_0 represents the internal resistance of the same battery cell. Consequently, Eq. (2) is simplified to

$$Q_z = \frac{I^2 R_0}{V_b}. \tag{3}$$

The total solar radiation heat absorbed by the battery pack, denoted as $Q_{sun} = \sum Q_{sun,i}$, is estimated by summing the incident direct solar irradiance I_{ZS} and the incident diffuse solar irradiance I_{SS}. That is, $Q_{sun} = I_{ZS} + I_{SS}$.

(1) Incident direct solar irradiance I_{ZS}

The calculation formula is presented as[28]

$$\sin H = \sin\beta\sin\alpha + \cos\beta\cos\alpha\cos\omega\,, \tag{4}$$

$$I_{ZS} = I_S \sin H\,. \tag{5}$$

In Eqs. (4) and (5), H denotes the solar altitude angle, β is the geographic latitude, α is the solar declination angle, and ω represents the hour angle. Conventionally, ω is expressed over a 24 h cycle, mapped linearly to the angular range of 0 to 360°, where 1 h corresponds to 15° and 1 min to 15′. In this study, however, ω is defined over the symmetric interval [−180°, +180°], with −180° corresponding to 00:00 (midnight), 0° to 12:00 (noon), and +180° to 24:00 (midnight), thereby facilitating trigonometric symmetry and simplifying computational implementation. I_S represents the direct beam solar irradiance incident on a horizontal surface, united in $W{\cdot}m^{-2}$.

(2) Incident diffuse solar irradiance, I_{SS}

According to the ASHRAE model, which is the heating and cooling calculation model developed by the American Society of Heating, Refrigerating and Air-conditioning Engineers, the incident diffuse solar irradiance I_{SS} on a vertical surface under a sunny sky is determined as follows.[29,30] Specifically, the calculation begins with the ratio of diffuse irradiance on a vertical surface I_{dv} to that on a horizontal surface I_{dH}, i.e., I_{dv}/I_{dH}.

$$\frac{I_{dv}}{I_{dH}} = \begin{cases} 0.55 + 0.437\cos\theta + 0.313\cos^2\theta, & \cos\theta > 0.2 \\ 0.45, & \cos\theta \le 0.2 \end{cases} \tag{6}$$

In Eq. (6), θ denotes the angle of incidence, which is the angle between the incident sunlight ray and the surface normal. Then, the incident diffuse solar irradiance on the vertical plane is calculated as

$$I_{SS} = \frac{I_{dv}}{I_{dH}} k I_{ZS}\,. \tag{7}$$

In Eq. (7), k denotes the ratio of horizontally incident solar diffuse radiation to direct normal irradiance. This parameter is typically determined through field measurements combined with iterative regression analysis.[29,30]

The incident solar diffuse radiation on nonvertical surfaces can be evaluated as

$$I_{SS} = k I_{ZS}\left(\frac{1+\cos\gamma}{2}\right), \tag{8}$$

where γ denotes the angle between the computed nonhorizontal plane and the reference horizontal plane.

By integrating the total heat transfer within the battery pack with the incident solar radiation heat absorbed by the pack, the heat transfer model for the grid cells of the lithium-ion battery pack can be reformulated accordingly.

$$m_i c_i \frac{dT_i}{dt} = Q_{sun} + Q_z + \left[Q_{rad,i}(t) + Q_{cond,i}(t) + Q_{conv,i}(t) \right] \tag{9}$$

Here, Q_{sun} is the total incident solar radiation. Q_Z is the total heat transfer per unit volume of the battery pack. $Q_{rad,i}(t) + Q_{cond,i}(t) + Q_{conv,i}(t)$ represents the net heat transfer at the *i*th grid cell, which incorporates radiation, conduction, and convection with internal and external environments. Positive net heat accumulation raises battery temperature, whereas negative net heat accumulation lowers it. These terms collectively describe the thermal energy balance of the battery pack.

2.2 Simulating configurations of liquid-cooling battery packs

The computational platform employed in this study comprises an Intel Core i9-14900K workstation equipped with 32 GB of DDR5 RAM and a GPU featuring 12 GB of dedicated video memory. Numerical simulations were conducted using the ANSYS Fluent module version 2023 R1. The computational domain was discretized into three distinct subdomains, that is, the power battery pack, the embedded liquid-cooling channels, and the surrounding fluid domain. Solar radiation effects were modeled using the Discrete Ordinates (DO) radiation model. The pressure–velocity coupling algorithm adopted was the Semi-implicit Method for Pressure-Linked Equations (SIMPLE). Under-relaxation factors were set to 0.5 for turbulent kinetic energy, 0.5 for turbulent dissipation rate, 0.2 for pressure, and 0.5 for momentum. To ensure solution convergence and numerical robustness, residual thresholds were specified as 1×10^{-5} for both the continuity and momentum equations, and 1×10^{-6} for the energy equation.

For mesh discretization, tetrahedral elements are assigned to highly intricate zones of the battery assembly, especially confined interstitial spaces and acute-angle interfaces between cells and coolant channels, to faithfully capture fine geometric features. Conversely, hexahedral elements are applied to all flow regions, including both inside and outside the pack, owing to their superior convergence behavior and solution precision in computational fluid dynamics.

Since thermal management involves simultaneous radiation, conduction, and convection processes, a composite meshing approach integrating both element types is implemented to simultaneously satisfy modeling accuracy and solver stability requirements. Two solar irradiation scenarios are modeled: one without active cooling and the other incorporating liquid-based thermal regulation; their respective computational domains are depicted in Figs. 1 and 2, respectively. Independent meshing is conducted for each scenario, producing meshes comprising 1.60×10^6 elements with a minimum quality metric of 0.852 and 2.43×10^6 elements with a minimum quality metric of 0.837, respectively.

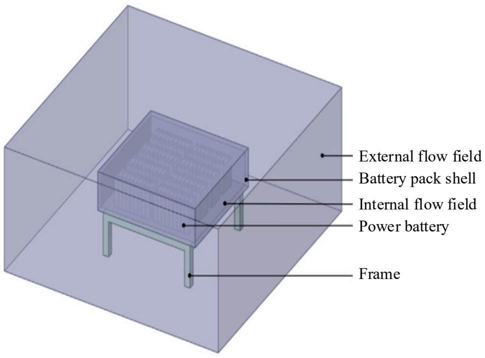

Fig. 1. (Color online) Solar radiation model without liquid cooling.

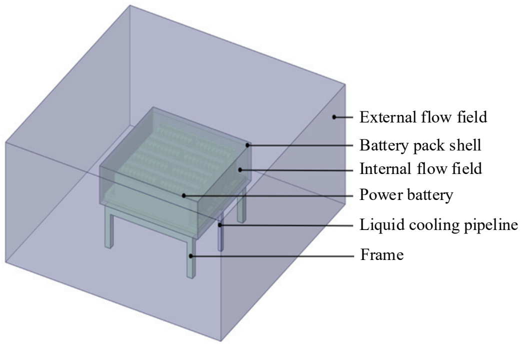

Fig. 2. (Color online) Liquid-cooling solar radiation model.

In this study, the battery pack model employs LF105 $LiFePO_4$ cells and is characterized by a nominal operating voltage of 3.2 V and a rated capacity of 105 Ah. Each cell has a rectangular geometry measuring 130 mm in length, 36 mm in width, and 200 mm in height, with an associated mass of 1.98 kg. key thermophysical properties are defined as follows: density of 2070 kg/m^3, specific heat capacity of 1060 J/(kg·K), and directional thermal conductivities of 31 W/(m·K) in the x-direction, 0.8 W/(m·K) in the y-direction, and 31 W/(m·K) in the z-direction.[23–25,31,32] For auxiliary components, namely, the case of the pack, cooling channels, surrounding and internal fluid regions, and heat transfer medium, material assignments are based on default entries in the simulation platform's native material library. The case of the pack is assigned the properties of structural steel; the cooling tubes, those of aluminum; the fluid domains in both external ambient and internal passages, those of air; and the circulating coolant, those of liquid water.

The propulsion battery system employed in EVs is engineered to enable a minimum operational range of 200 km under typical driving scenarios. To fulfill this requirement, the battery pack's energy rating is set at no less than 22 kWh. Cell-level implementation utilizes $LiFePO_4$ cells organized into a hierarchical structure. Each module consists of nine cells connected in series, and eight of these modules are subsequently linked in series to assemble the complete battery assembly, thereby incorporating exactly 72 cells. This arrangement delivers a nominal output voltage of 230.4 V and a rated charge capacity of 105 Ah, corresponding to an aggregate stored energy of roughly 24.2 kWh. A schematic representation of the pack's structural organization and physical dimensions is provided in Fig. 1.

2.3 Specification of boundary conditions

At discharge rates of 1, 1.5, and 2C, the battery delivers currents of 105, 157.5, and 210 A, respectively. Using Eq. (3), we determined the associated volumetric heat production under these conditions to be 3769, 8481, and 15077 W/m^3, respectively.

Thermal interactions at the interfaces among the battery module, its case, and the rack structure are represented through conjugate heat transfer boundary formulations. Radiation exchange with the surroundings is imposed on the outermost surface of the computational domain. Two ambient temperature scenarios are considered, that is, 25 °C for baseline thermal analysis and 35 °C for high-temperature operational assessment. A defined external radiation coefficient governs this surface exchange. In the radiative heat transfer model, boundaries exhibiting partial optical transparency are assigned a semitransparent radiation type, with their respective transmittance and absorption properties individually specified.

Conjugate heat transfer conditions are further implemented across all thermally interacting components, including the battery cell assembly, case of the pack, support rack, liquid-cooling plate, internal cavity, and base plate, with interfacial regions treated as fully coupled thermal domains. Within the internal cavity, radiation behavior is modeled assuming semitransparency, while all remaining boundaries are treated as nontransmissive, i.e., opaque. Key radiative properties, including emissivity, transmittance, and absorption, have been assigned on the basis of material-specific data, as compiled in Table 1.(19,33,34)

Within the external flow region, the outflow boundary is modeled using a pressure outlet condition, maintained at a constant static temperature of 298 K. Regarding radiative heat transfer, both the inlet and outlet boundaries are treated as semitransparent surfaces, each assigned a solar transmissivity of 0.8. All other radiation-related parameters are left unchanged from their default settings. At the inflow boundary, a velocity inlet condition is applied, imposing a steady incoming flow velocity of 1 m/s and a uniform static temperature of 298 K. The numerical simulation is conducted in the transient mode, comprising 100 steps, with each step spanning 36 s. Moreover, all additional solver options are kept at the default values.

3. Numerical Simulations and Discussion

Existing literature(4–8) largely overlooks the combined effects of solar irradiation and ground-reflected radiation on the thermal performance of lithium-ion battery packs, especially when liquid cooling is employed for thermal regulation. To address this oversight, in the present work, we begin with a computational investigation into how direct and reflected solar fluxes affect the spatial temperature profile within the battery module. A key contribution lies in explicitly accounting for albedo-induced radiation in the thermal model, a factor often neglected in prior

Table 1
Boundary conditions for solar radiation

Component	Emissivity	Absorptivity	Transmissivity
Battery cell	0.4	0.8	0
Case of pack	0.82	0.8	0
External flow region	0.9	0.15	0.8
Support rack	0.82	0.8	0
Liquid-cooling plate	0.55	0.3	0
Base plate	0.94	0.74	0

solar-exposure studies, supported by detailed simulation protocols and quantitative outcomes. Finally, in this study, we contrast the equilibrium thermal responses of two configurations, that is, battery assemblies operating without active cooling and those equipped with embedded liquid-cooling components.

3.1 Effect of ground radiation

Figure 3 shows the thermal distribution across the battery pack under a solar radiation model that excludes ground-reflected components. In contrast, Fig. 4 depicts the resulting temperature field when the model accounts for albedo effects from the underlying surface. Figure 5 provides a side-by-side analysis of core and surface temperature responses for both configurations.

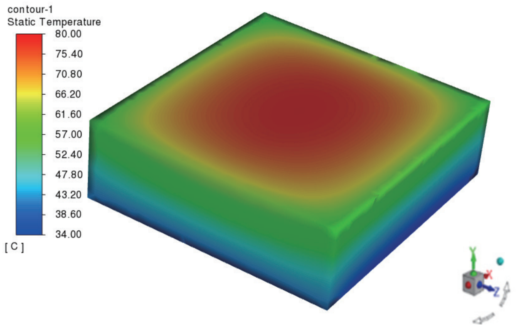

Fig. 3. (Color online) Temperature distribution without ground reflection.

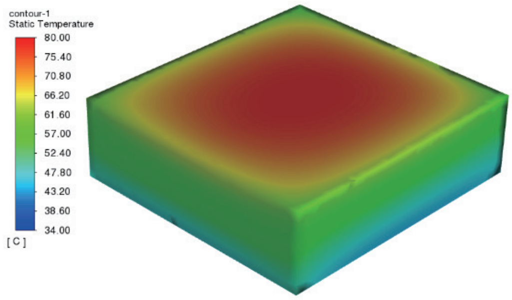

Fig. 4. (Color online) Temperature distribution with ground reflection.

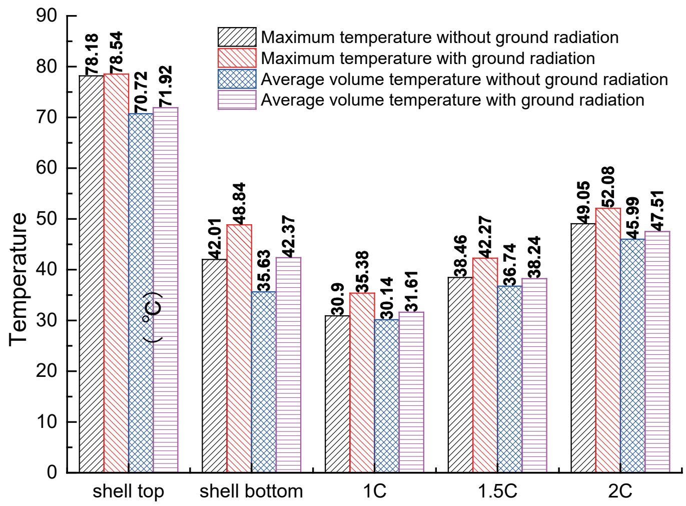

Fig. 5. (Color online) Internal and external temperatures with and without ground reflection effects.

The numerical results are examined and described below referring to Fig. 5.

1 Figure 5 shows that ground radiation significantly raises temperatures at the battery enclosure's base (+6.74 ℃) and sidewalls (+2.71 ℃) under 25 ℃ ambient conditions, primarily via direct infrared transfer and reflection-induced re-emission.

2 Ground radiation increases peak cell temperature, but this effect weakens with higher discharge rates; at 1C, peak and average internal temperatures rise by 4.48 and 1.47 ℃, respectively.

3 Because of preferential outward heat dissipation and convection with radiation, which restricts inward conduction to the cells, the enclosure's exterior is constantly hotter than its interior.

In summary, ground radiation plays a critical role in shaping the battery pack's thermal response by altering its radiative exchange and surface reflectivity, which in turn modifies heat distribution both within the pack and across its boundaries. As such, ignoring ground-reflected irradiance in the thermal modeling of EV battery systems exposed to sunlight introduces notable inaccuracies and should be avoided in rigorous simulation frameworks.

3.2 Solar thermal analysis of power battery packs

In this study, we applied the computational simulation to examine the integrated thermal and fluid behaviors of a power battery pack. Three key modeling assumptions were adopted. (1) Battery cells were modeled as uniform volumetric heat sources with temperature-invariant thermophysical properties. (2) Heat generation was assumed to be steady and temperature-independent. (3) Gauge pressure was set to zero for all domains, including ambient air, internal cooling channels, and coolant, using atmospheric pressure as a reference.

The thermal simulation incorporated solar irradiation onto the battery assembly by employing the DO method for radiative heat transfer, coupled with dynamic solar position tracking. Key environmental inputs for the irradiation solver included the following: a geographic location at 117.5644° east longitude and 26.19272° north latitude, a local time reference of UTC+8, and a simulation timestamp of 13:00 on June 21. A right-handed Cartesian coordinate system was adopted, where the global north vector coincided with the $-z$ direction (0, 0, −1) and the east vector aligned with the $+x$ direction (1, 0, 0). To represent ideal atmospheric transmission, the model assumed unobstructed sky conditions, assigning a dimensionless clear-sky transmissivity of unity.

Figure 6 depicts how solar radiation intensity varies spatially over the surface of the battery pack enclosure. Corresponding thermal distributions, represented as color-coded temperature fields, are shown in Fig. 7 (at 25 ℃ ambient) and Fig. 8 (at 35 ℃ ambient), reflecting the enclosure's thermal response under two distinct environmental temperature settings.

The numerical results from Fig. 6 are examined and explained below.

1 Solar irradiance peaks to 611.24 W/m^2 on the battery pack's top surface, and the shell temperature rises to 69.29 ℃ at 25 ℃ ambient and to 79.68 ℃ at 35 ℃ ambient.

2 The negative x-axis-acing surface receives the second-highest irradiance to 394.31 W/m^2 owing to optimal solar alignment at 13:00, as indicated by the solar direction vector given by (−0.192829, 0.980458, 0.0389779).

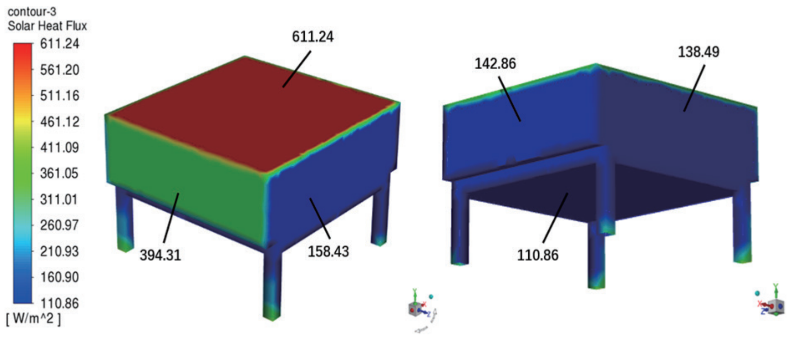

(a) (b)

Fig. 6. (Color online) Solar radiation intensity distribution of the case of the pack. (a) Top view. (b) Side view.

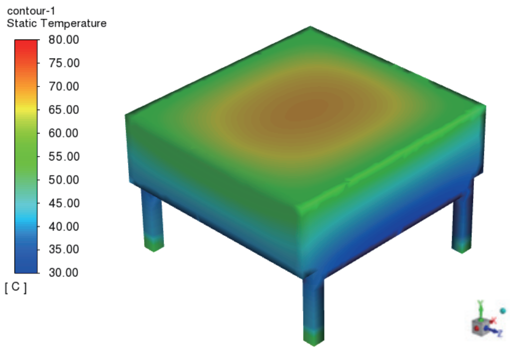

Fig. 7. (Color online) Temperature distribution of the case of the pack at 25 °C.

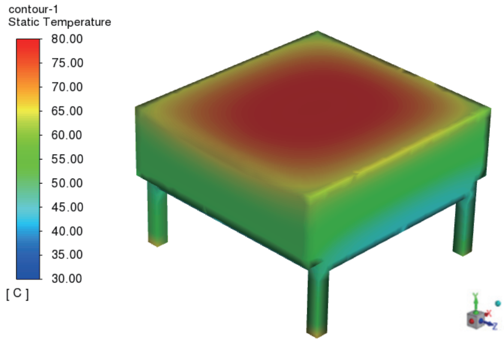

Fig. 8. (Color online) Temperature distribution of the case of the pack at 35 °C.

3 All other surfaces receive only diffuse radiation from atmospheric scattering, leading to substantially lower irradiance values.

3.3 Steady-state flow analysis of power battery pack

The battery pack enclosure exchanges heat with its surroundings via four mechanisms, namely, solar irradiation, thermal radiation, convection, and conduction. Solar irradiation is the main heat gain source, whereas heat loss occurs only through radiation, convection, and conduction, excluding solar input. A positive net heat flux indicates heating; its magnitude determines the heating rate. A negative net heat flux indicates cooling; larger negative values mean faster cooling. Figure 9 shows the airflow velocity distribution on the side, top, and bottom surfaces.

Figure 9 also shows elevated airflow velocities at the top, bottom, and side surfaces of the power battery pack, with the peak velocity at the top. Vortices form on the side walls, rear panel, and upper region. They result from airflow expanding radially after impacting the front surface, creating low-pressure zones that induce reverse flow and rotation. Although present, these

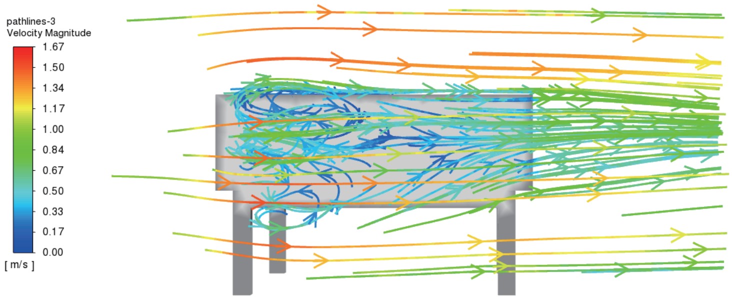

Fig. 9. (Color online) Distribution of the external flow field around the power battery pack.

vortices have low kinetic energy. Consequently, their effect on the battery pack's thermal performance is negligible.

3.4 Thermal analysis of liquid-cooling battery packs at different discharge rates

In this section, we investigate how solar irradiance affects the thermal response of the battery pack. To assess the impact of cooling intervention, two distinct numerical models are developed and analyzed. (1) The reference model represents the unmodified battery pack operating without active thermal management. (2) The enhanced model features an embedded liquid-cooling plate labeled Case 1. A steady-state thermal evaluation is then carried out to quantify and contrast key temperature metrics, including maximum cell temperature and spatial temperature uniformity, across both setups.

As depicted in Fig. 10, Case 1 features a specific arrangement of inlet and outlet ports for the coolant circuit integrated within the pack. At the system's discharge end, a pressure-outlet boundary condition is applied, with the reference thermodynamic temperature fixed at 298 K, and no modifications are made to the remaining solver configurations. Moreover, the ambient airflow entering the external domain is modeled using a velocity-inlet boundary condition, imposing a constant inflow speed of 0.4 m/s and a uniform static temperature of 298 K; all other associated parameters are left unchanged from their factory-default values.

Thermal profiling using carefully selected planar sections enables the thorough evaluation of temperature gradients in the battery pack. It identifies localized heat distribution differences and quantifies thermal nonuniformity. The analysis planes are geometrically optimized for accurate thermal assessment. Their schematic layout is shown in Fig. 11. This method supports precise, spatially resolved thermal characterization.

In summary, the numerical results from Fig. 12 are examined and discussed below.

1 Figure 12 demonstrates that solar irradiation induces a sequential thermal response in the power battery pack. First, the outer enclosure heats up owing to direct exposure. Subsequently, heat propagates inward through conduction, causing a sustained rise in core

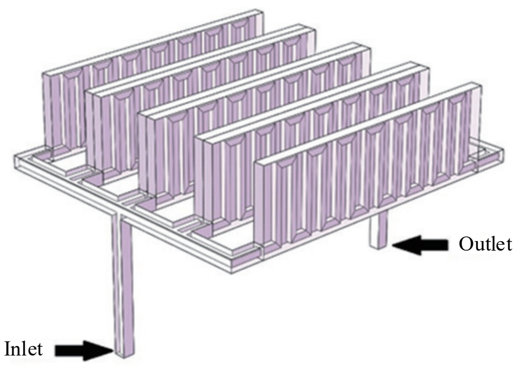

Fig. 10. (Color online) Inlet and outlet configurations of the liquid-cooling system (Case 1).

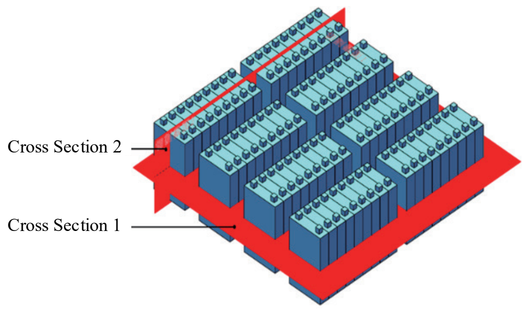

Fig. 11. (Color online) Cross sections of the power battery pack.

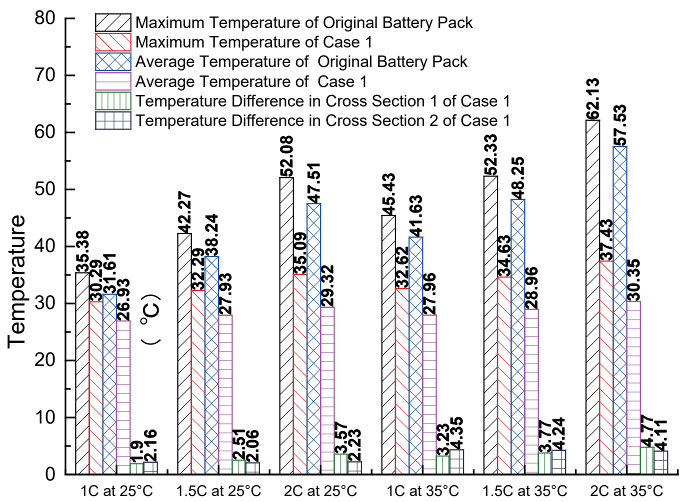

Fig. 12. (Color online) Comparative cooling performance of Case 1 at 25 and 35 °C.

module temperature. When ambient temperature increases from the reference level of 25 to 35 °C, the combined effects of the upward long-wave radiation from the ground and the trapped internal radiation intensify, while natural convection at the pack surface weakens. As a result, the peak temperature of the battery assembly climbs to 62.13 °C after 60 min of continuous operation.

2 In Case 1, increasing the battery's discharge current leads to a larger net temperature drop facilitated by the liquid-cooling plate, suggesting improved cooling capacity under higher thermal loads. Nevertheless, overly aggressive cooling may widen the temperature spread across Sect. 1, thereby reducing thermal homogeneity within that plane.

3 As the coolant traverses the liquid-cooling loop and extracts thermal energy from two neighboring battery modules, its enthalpy rises progressively in the flow direction. This results in a distinct inlet-to-outlet temperature differential, with the lowest temperature observed at the inlet and the highest at the outlet. Such a longitudinal thermal variation is distinctly visible in the temperature distribution visualizations for both cross sections 1 and 2.

4 For Case 1, raising the ambient temperature from 25 to 35 ℃ leads to a substantially higher baseline operating temperature for the battery pack. Consequently, the cooling system delivers a greater absolute temperature decrease, indicating improved performance but a higher thermal load necessitating more significant heat removal.

4. Improvement Design and Analysis of Liquid-cooling Systems for Battery Packs

With Case 1, the battery pack exhibited notable reductions in both peak and mean temperatures. However, temperature gradients among individual cells remained pronounced. To achieve further thermal management enhancement, specifically targeting a lower average module temperature, a novel liquid-cooling plate design, Case 2, was introduced in this section. Figure 13 presents the geometric configuration of the Case 2 plate, which utilizes an integrated flow path architecture combining sequential and branched coolant passages. The system incorporates two fluid inlets and one outlet. Compared with Case 1, the total count of cooling plates increased from eight to sixteen, thereby expanding the surface-area contact and improving the localized heat removal. Additionally, the port arrangement was revised: instead of one inlet and one outlet, the updated design adopts two inlets feeding into a shared outlet. Collectively, these engineering refinements led to more balanced coolant flow distribution and a marked increase in thermal dissipation performance, especially in regions located farthest from the primary coolant entry points.

The simulation was conducted under controlled thermal and aerodynamic conditions with an ambient temperature of 35 ℃ and a freestream wind velocity of 1.0 m/s. For the coolant circuit, the outlet boundary was defined using a pressure-outlet condition. Moreover, the external airflow entered the domain through a velocity-inlet boundary with a fixed temperature of 298 K and a constant inflow speed of 0.4 m/s. Turbulence intensity, thermal wall functions, and other solver-specific parameters were retained at their built-in defaults unless explicitly specified. The thermal response characteristics of the battery module with Case 2 are summarized in Fig. 14.

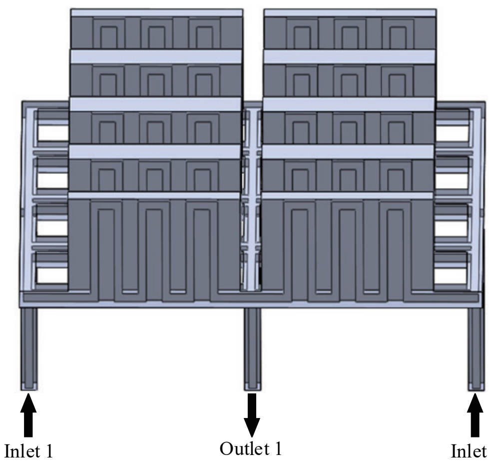

Fig. 13. (Color online) Enhanced liquid-cooling plate configuration of Case 2.

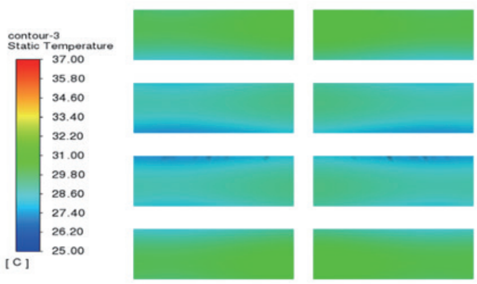

Fig. 14. (Color online) Temperature distribution of cross section 1 (2C rate) with Case 2.

To evaluate thermal consistency across designs, Figs. 15–17 provide side-by-side presentations of the data for the original pack, Case 1, and Case 2 using three key indicators, namely, peak cell temperature, spatially averaged temperature, and the temperature difference between the highest and lowest cell temperatures.

The numerical results are analyzed and interpreted in the following discussion, with supporting illustrations provided in Figs. 15–17.

1 At an ambient temperature of 25 ℃, Case 1 and Case 2 demonstrated peak temperature reductions of 32.62 and 33.22%, respectively, when benchmarked against the reference battery configuration. Similarly, their mean volumetric temperatures respectively dropped by 38.29 and 39.53% relative to the same reference.

2 When tested at an ambient temperature of 35 ℃, both configurations further improved thermal performance. Case 1 and Case 2 have reduced maximum temperatures by 39.76 and 40.91%, respectively. Compared with the reference pack, their average volumetric temperatures fell by 47.24 and 48.64%, respectively.

3 Operating at a 2C discharge rate under 35 ℃ ambient conditions, Case 2 delivered a direct peak temperature decrease of 25.42 °C and a mean volumetric temperature drop of 27.98 ℃

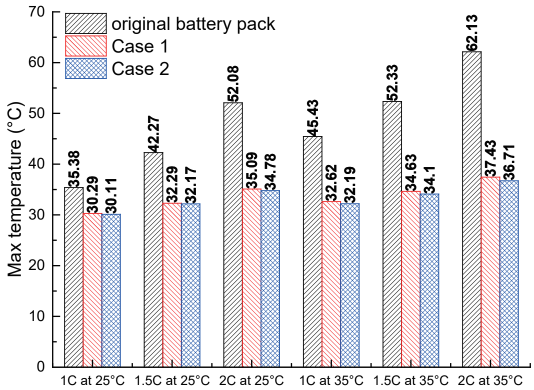

Fig. 15. (Color online) Maximum operating temperatures of original battery pack, Case 1, and Case 2.

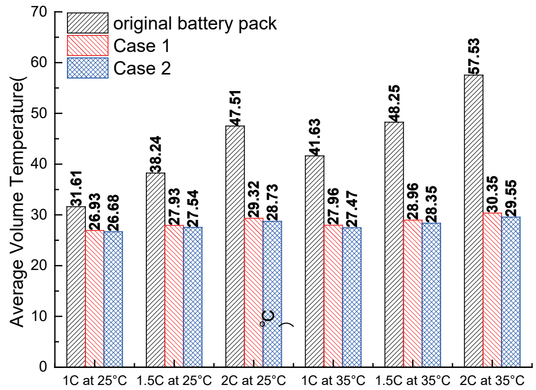

Fig. 16. (Color online) Average volume temperatures of original battery pack, Case 1, and Case 2.

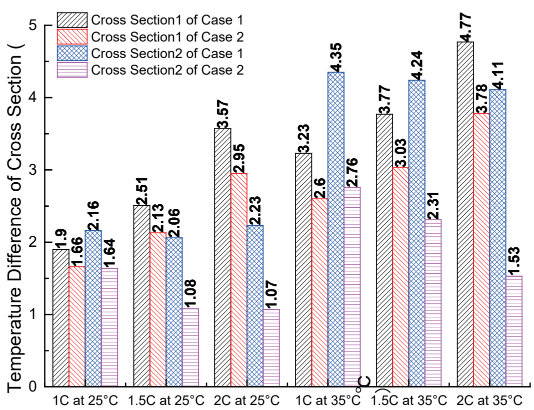

Fig. 17. (Color online) Temperature differences at cross sections of battery pack at 25 and 35 ℃.

versus the baseline. Spatial temperature analysis revealed a 3.78 ℃ differential between cross sections 1 and 2, and a 1.53 ℃ difference between cross section 2 and the underlying liquid-cooling surface.

4 Under 25 ℃ ambient conditions, Case 2 reduced the thermal disparity between cross sections 1 and 2 by 17.37%, and the gap between cross section 2 and the liquid-cooling plate by 52.02%, relative to Case 1. These improvements were more pronounced at 35 ℃, with corresponding reductions of 20.75 and 62.77%, respectively.

5 The enhanced thermal management in Case 2 stems from structural modifications, an increased number of coolant inlets and additional liquid-cooling plates, which collectively minimize flow path length in the front and rear zones. This refinement curbs localized coolant heating and flattens the axial temperature distribution across the cooling plate, leading to markedly lower temperature variations among internal sections and superior overall thermal homogeneity within the battery assembly.

In summary, the Case 2 battery pack meets all key performance requirements under normal operating conditions. Its thermal management outperforms both the original package and Case 1 designs. Specifically, it achieves better heat dissipation and more uniform cross-sectional temperature distribution. These improvements enhance system reliability. They also boost the overall functional efficiency of the power battery.

5. Conclusions

In this study, we built a physics-driven thermal model of a solar-irradiated battery module and compared two liquid-cooling layouts. We identified the following key findings: (1) The pronounced longitudinal temperature gradient arises from nonuniform cooling along the flow path. (2) The rapid temperature increase during high-current discharge is primarily attributable to elevated electrochemical losses. (3) Solar heating elevates the casing temperature to as high as 79 ℃, thereby driving inward heat conduction and resulting in higher temperatures within the cell layers. (4) The inlet geometry was optimized by increasing its cross-sectional area and shortening the front and rear flow paths, which effectively mitigates axial temperature variation.

We also proposed a numerical simulation method to replace year-long outdoor aging tests for EV battery thermal and degradation evaluation. We accurately predicted intracell and pack-level heat transfer under varying solar and thermal conditions. The model enables the rational selection of irradiance and temperature profiles for accelerated testing. As a result, we considerably reduced the test duration, labor, and resource use. This approach provides a practical, time-efficient alternative to traditional natural exposure trials.

Acknowledgments

This work was carried out as part of the Major Science and Technology Projects of Fujian Province (Grant No. 2023T5001), the Operational Funding of the Advanced Talents for Scientific Research (Grant No. 19YG04) of Sanming University, and the Natural Science Foundation of Sanming University (Grant No. KD23003P). The authors also acknowledge the support from the School of Mechanical and Electric Engineering, Sanming University.

References

1 Y. Ortiz, P. Arévalo, D. Peña, and F. Jurado: Batteries **10** (2024) 83. https://doi.org/10.3390/batteries10030083
2 Q. L. Yue, C. X. He, M. C. Wu, and T. S. Zhao: Int. J. Heat. Mass. Transf. **181** (2021) 121853. https://doi.org/10.1016/j.ijheatmasstransfer.2021.121853
3 K. Y. Gómez Díaz, L. De, S. E. Aldaco, J. Aguayo Alquicira, M. Ponce Silva, S. Portillo Contreras, and O. Sánchez Vargas: World Electr. Veh. J. **16** (2025) 346. https://doi.org/10.3390/wevj16070346
4 N. Vinten, O. Jianu, A. El-Sharkawy, and D. Arora: Energy Technol. **13** (2025) 2401331. https://doi.org/10.1002/ente.202401331
5 Y. Tan, Y. Li, Y. Gu, W. Liu, J. Fang, and C. Pan: Energies **17** (2024) 178. https://doi.org/10.3390/en17010178
6 Y. Fan, Z. Wang, X. Xiong, J. Zhu, Q. Gao, H. Wang, and H. Wu: Appl. Therm. Eng. **220** (2023) 119680. https://doi.org/10.1016/j.applthermaleng.2022.119680
7 M. Li, J. Wang, Q. Guo, Y. Li, Q. Xue, and G. Qin: J. Energy Eng. **146** (2020) 04020037. https://ascelibrary.org/doi/pdf/10.1061/(ASCE)EY.1943-7897.0000648
8 N. Indraneel and N. Milankumar: Energy Technol. **9** (2021) 59. https://doi.org/10.1002/ente.202100593
9 M. Schreiber, L. L. Köning, G. Balke, K. A. Gamra, J. Kayl, B. Dietermann, R. Urban, C. Grosu, and M. Lienkamp: eTransp. **27** (2026) 100518. https://doi.org/10.1016/j.etran.2025.100518
10 J. de la Vega Hernández, J. A. Ortega-Redondo, and J. R. Riba: Sci. Data **12** (2025) 1942. https://doi.org/10.1038/s41597-025-06229-5
11 S. Pakštys, M. Maritano, F. Boscarino, and A. Bonfitto: J. Energy Storage **153** (2026) 120424. https://doi.org/10.1016/j.est.2026.120424
12 C. Xu, Q. Chen, S. Liu, C. Zhong, C. Wan, and X. Yu: Appl. Therm. Eng. **282** (2026) 128800. https://doi.org/10.1016/j.applthermaleng.2025.128800
13 F. Falcone, A. Giannotta, R. Ricco, and P. De Palma: Appl. Therm. Eng. **279** (2025) 127575. https://doi.org/10.1016/j.applthermaleng.2025.127575
14 SAE Technical Report No. J2412-202402 (2024). https://www.sae.org/standards/content/j2412_202402/
15 SAE Technical Report No. J2527-201706 (2017). https://doi.org/10.4271/J2527_201706
16 J. Feng, F. Cai, X. Zhan, K. Huang, S. Wang, and X. Zhang: Meas. Part B **242** (2025) 115982. https://doi.org/10.1016/j.measurement.2024.115982
17 W. Li, Y. Xie, R. Yang, Y. Fan, K. Zhang, and S. Panchal: IEEE Trans. Ind. Electron. **72** (2025) 10257. https://doi.org/10.1109/TIE.2025.3555004
18 D. Chen, Q. Zhao, Y. Zheng, Y. Xu, Y. Chen, J. Ni, and Y. Zhao: Sensors **23** (2023) 5609. https://doi.org/10.3390/s23125609
19 G. Kovács, S. Kocsis Szürke, and S. Fischer: Batteries **11** (2025) 246. https://doi.org/10.3390/batteries11070246
20 K. Kumba, S. P. Simon, V. Gundu, P. Upender, N. Ra, and M. Sarkar: IEEE Access **12** (2024) 33720. https://doi.org/10.1109/access.2024.3369914
21 F. Wang and C. You: Energy Rep. **8** (2022) 245. https://doi.org/10.1016/j.egyr.2021.11.028
22 Z. Tang, A. Song, S. Wang, J. Cheng, and C. Tao: Energies **13** (2020) 1010. https://doi.org/10.3390/en13041010
23 S. Zeinali and E. Neshat: Case Stud. Therm. Eng. **74** (2025) 106732. https://doi.org/10.1016/j.csite.2025.106732
24 B. Wang, C. Z. Jiao, and S. H. Zhang: Energies **18** (2025) 2406. https://doi.org/10.3390/en18092406
25 M. Xiong, N. Wang, W. Li, A. Garg, and L. Gao: Batteries **9** (2023) 44. https://doi.org/10.3390/batteries9010044
26 M. Murphy and M. Akrami: Batteries **10** (2024) 264. https://doi.org/10.3390/batteries10080264
27 R. Banerjee and K. Nidhul: Results Eng. **26** (2025) 104688. https://doi.org/10.1016/j.rineng.2025.104688
28 J. Appelbaum and A. Peled: Urban Sci. **9** (2025) 211. https://doi.org/10.3390/urbansci9060211
29 A. Aronescu and J. Appelbaum: Energies **14** (2021) 2245. https://doi.org/10.3390/en14082245
30 R. E. Sánchez-García, R. Salmón-Folgueras, O. Castilleja-Escobedo, and J. L. López-Salinas: Results Eng. **26** (2025) 105207. https://doi.org/10.1016/j.rineng.2025.105207
31 J. Kim, C. Yang, J. Lamb, A. Kurzawski, J. Hewson, L. Torres-Castro, A. Mallarapu, and S. Santhanagopalan: J. Electrochem. Soc. **169** (2022) 110543. https://doi.org/10.1149/1945-7111/ac9ee4
32 D. Ganesan, V. R. Madhavan, and V. Ramalingam: Therm. Sci. Part A **28** (2024) 1. https://doi.org/10.2298/TSCI230110081G
33 Y. Gao, F. Qiao, W. Hou, L. Ma, N. Li, C. Shen, T. Jin, and K. Xie: Innovation **4** (2023) 100468. https://doi.org/10.1016/j.xinn.2023.100468
34 A. Bacak: Inst. Mech. Eng., Part D: J. Automob. Eng. **239** (2025) 2461. https://doi.org/10.1177/09544070241242825